

Faraday instability on a sphere: numerical simulation

A. Ebo Adou^{1,2}, L.S. Tuckerman¹ †, S. Shin³, J. Chergui² and
D. Juric²

¹Laboratoire de Physique et Mécanique des Milieux Hétérogènes (PMMH), UMR CNRS 7636 ; PSL-ESPCI; Sorbonne Univ.- UPMC, Univ. Paris 6; Sorbonne Paris Cité-UDD, Univ. Paris 7

²LIMSI, CNRS, Université Paris-Saclay, 91405 Orsay, France

³Department of Mechanical and System Design Engineering, Hongik University, Seoul 121-791, Republic of Korea

(Received xx; revised xx; accepted xx)

We consider a spherical variant of the Faraday problem, in which a spherical drop is subjected to a time-periodic bulk force, as well as surface tension. We use a full three-dimensional parallel front-tracking code to calculate the interface motion of the parametrically forced oscillating viscous drop, as well as the velocity field inside and outside the drop. Forcing frequencies are chosen so as to excite spherical harmonic wavenumbers ranging from 1 to 6. We excite gravity waves for wavenumbers 1 and 2 and observe translational and oblate-prolate oscillation, respectively. For wavenumbers 3 to 6, we excite capillary waves and observe patterns analogous to the Platonic solids. For this low-viscosity case, both subharmonic and harmonic responses are accessible. The patterns arising in each case are interpreted in the context of the theory of pattern formation with spherical symmetry.

1. Introduction

The Faraday (1831) instability, in which the interface between two superposed fluid layers subjected to periodic vertical vibration of sufficient amplitude forms sustained standing wave patterns, has been instrumental in the study of pattern formation, leading to the discovery and analysis of hydrodynamic quasipatterns (Edwards & Fauve 1994; Rucklidge & Skeldon 2015), superlattices (Kudrolli *et al.* 1998; Silber & Proctor 1998; Arbell & Fineberg 2002), supersquares (Douady 1990; Kahouadji *et al.* 2015) and other exotic patterns (Périnet *et al.* 2012; Rajchenbach *et al.* 2011).

Here, we consider a spherical analogue to the Faraday instability, that of a fluid drop subjected to a time-periodic radial bulk force. The laboratory realization of any configuration with only spherically symmetric radially directed forces is difficult, if not impossible. Indeed such experiments are sent into space (Wang *et al.* 1996; Fütterer *et al.* 2013) in order to eliminate or reduce the perturbing influence of the vertically directed gravitational field of the Earth. Investigations of acoustically levitated drops excited by electric modulation (Shen *et al.* 2010) or of drops and puddles weakly pinned on a vibrating substrate (Brunet & Snoeijer 2011) have produced star-like patterns, but in both configurations the basic state is necessarily oblate rather than spherical. The study of such problems therefore relies particularly on numerical simulation.

Numerical studies of axisymmetric oscillating viscous drops have been carried out by Lundgren & Mansour (1988) via a boundary-integral method, by Patzek *et al.* (1991) and

† Email address for correspondence: laurette@pmmh.espci.fr

Meradji *et al.* (2001) via a Galerkin/finite-element method, and by Basaran (1992) via a marker-in-cell initial-value problem. Indeed, the problem of axisymmetric ellipsoidal drop oscillation and decay has now come to be seen as a routine validation test case for numerical codes and interface methods for multiphase flows. However, the full non-linear problem is non-axisymmetric and requires three-dimensional numerical simulation with interface algorithms that ensure volume conservation and precise calculation of capillary forces as well as the ability to integrate highly spatially resolved systems over long physical times.

Recent advances have led to powerful general purpose codes such as Popinet’s Gerris code (Popinet 1993) and BLUE (Shin *et al.* 2015). It is with the multiphase code BLUE, which is based on recently developed front-tracking interface methods implemented on parallel computer architectures, that we conduct the current study. We have previously used this code to study large-scale square patterns of Faraday waves (Kahouadji *et al.* 2015). Here, we use BLUE to carry out the first numerical investigation of the Faraday problem on a sphere.

One of the most appealing aspects of the Faraday instability is that the pattern length scale is not set by the geometry, but by the imposed forcing frequency. (It is this feature which has allowed the generation of quasipatterns and superlattices, since multiple length scales can be excited simultaneously over the entire domain by superposing different frequencies.) This means that for a drop with a fixed radius R , patterns can be created with any wavenumber ℓ , where the interface is described via its spherical harmonic decomposition

$$\zeta(t, \theta, \phi) = R + \sum_{\ell=1}^{\infty} \sum_{m=-\ell}^{m=\ell} \zeta_{\ell,m}(t) Y_{\ell}^m(\theta, \phi) \quad (1.1)$$

For fixed R , the length scale associated with ℓ is R/ℓ . More importantly, ℓ is associated with a set of allowed patterns; each value of ℓ leads to a qualitatively different situation. We will explore the motion and shape of an oscillating drop for values of ℓ up to 6.

2. Methods

2.1. Pattern formation on a sphere

Our companion paper (Ebo Adou & Tuckerman 2015) concerns the linear stability, via Floquet analysis, of the spherical Faraday problem. As is the case for all spherically symmetric problems, the equation governing the linear stability does not depend on the order m of the spherical harmonic. Therefore, a bifurcation from the spherically symmetric state involves $2\ell + 1$ linearly independent solutions (Y_{ℓ}^m with $-\ell \leq m \leq \ell$) with the same growth rate. The combination of these modes, i.e. the pattern, that can result from such a bifurcation is determined by the nonlinear terms. A pattern with a given ℓ cannot be associated with a unique combination of modes m , since rotation of a spherical harmonic changes m (but not ℓ). Spherical harmonics are sometimes classified as zonal ($m = 0$, independent of ϕ , nodal lines which are circles of constant latitude), sectoral ($m = \pm\ell$, independent of θ , nodal lines which are circles of constant longitude), or tesseral ($m \neq 0, \pm\ell$, checkered). This classification as well depends on the orientation of the spherical harmonic.

Symmetry groups provide a classification of patterns which does not depend on orientation. A number of researchers (Busse 1975; Busse & Riahi 1982; Riahi 1984; Ihrig & Golubitsky 1984; Golubitsky *et al.* 1988; Chossat *et al.* 1991; Matthews 2003) have studied the patterns which are allowed and those which are preferred for various

values of ℓ . Patterns that appear at bifurcations can be associated with a subgroup of the group $O(3)$ of symmetries of the sphere. The subgroups of interest are $O(2)$, D_m , and the exceptional subgroups T , O , and I . $O(2)$ consists of the symmetries of a circle; patterns which are axisymmetric (for some orientation) are in this category. D_k describes the symmetries of an k -gon, and thus patterns which are invariant under reflection and rotation by $2\pi/k$ (about a fixed axis). The three exceptional subgroups are associated with the five Platonic solids: T (tetrahedron), O (octahedron or cube), and I (icosahedron or dodecahedron).

The Platonic solids are regular polyhedra. Although a drop does not have angular vertices and flat faces, a polyhedron with the same symmetry properties can be constructed from a drop in a T , O , or I configuration by assigning a local maximum on the surface to a vertex and a local minimum to a face. The dual of a polyhedron is obtained by inverting its vertices with its faces, an operation which preserves symmetry. Similarly, the dual of a drop can be formed by inverting maxima and minima. An oscillating drop provides an ideal opportunity to observe duality: since a location which is the site of a maximum contains a minimum after half of an oscillation period, the interface alternates between a pattern and its dual. For the Platonic solids, the dual of an octahedron is a cube, that of an icosahedron is a dodecahedron and the dual of a tetrahedron is another tetrahedron.

The patterns are highly dependent on the value of ℓ considered. Axisymmetric (zonal) solutions are never stable if $\ell \geq 2$ (Chossat *et al.* 1991). For odd ℓ , solutions exist which are stable at onset. In contrast, for even ℓ , all solutions are unstable near the bifurcation point. In this case, the preferred solution is considered to be that with the smallest number of unstable eigenvalues (Matthews 2003). Unstable solution branches produced at a transcritical bifurcation can be stabilized, for example at a saddle-node bifurcation some distance from the threshold.

The theory of pattern selection with $O(3)$ symmetry differs from the framework of our simulations in some important ways. First, the theory applies to steady bifurcations rather than oscillatory solutions resulting from time-periodic forcing. The underlying application is usually Rayleigh-Bénard convection in a sphere (Busse 1975; Busse & Riahi 1982; Riahi 1984) and the steady symmetry-breaking bifurcations it undergoes. However, many of the conclusions can be generalized to the time-periodic context, by considering the discrete-time dynamical system derived by sampling the continuous-time system at a single phase of the forcing period.

A second difference is numerical: in particular, our simulations do not respect spherical symmetry. An initial set of simulations was carried out in a cubical domain, with a surrounding fluid whose density is much lower than that of the drop so as to minimize its effect on the drop. In order to correct this, and as our computational capabilities expanded, a solid bounding sphere was inscribed in the cubical domain, providing an approximation to a spherical boundary. Nonetheless, the Cartesian grid remains and continues to exert a cubical influence on our simulations.

Finally, the theory applies close to the threshold. Our simulations are carried out far from threshold, so that instabilities can grow on a reasonable timescale and stabilize at an amplitude that can be clearly seen. Our patterns contain modes generated by nonlinear interactions which are absent from the theory, and their existence or stability may result from secondary bifurcations.

Despite these differences, we will see that there is a great deal of common ground between the patterns we observe and those predicted by theory.

2.2. Problem formulation, governing equations and numerical scheme

The governing equations for an incompressible two-phase flow can be expressed by a single field formulation:

$$\rho \left(\frac{\partial \mathbf{u}}{\partial t} + \mathbf{u} \cdot \nabla \mathbf{u} \right) = -\nabla P + \rho \mathbf{G} + \nabla \cdot \mu (\nabla \mathbf{u} + \nabla \mathbf{u}^T) + \mathbf{F}, \quad \nabla \cdot \mathbf{u} = 0 \quad (2.1)$$

where \mathbf{u} is the velocity, P is the pressure, ρ is the density, μ is the dynamic viscosity and \mathbf{F} is the local surface tension force at the interface. Here, \mathbf{G} is an imposed time-dependent radial acceleration:

$$\mathbf{G} = -(g + a \cos(\omega t)) \frac{r}{R} \mathbf{e}_r \quad (2.2)$$

where g is a constant acceleration, referred to for simplicity as gravitational, \mathbf{e}_r is the radial unit vector, R is the radius of the drop, and a and ω are the amplitude and frequency of the oscillatory forcing.

Material properties such as density or viscosity are defined in the entire domain:

$$\begin{aligned} \rho(\mathbf{x}, t) &= \rho_1 + (\rho_2 - \rho_1) I(\mathbf{x}, t) \\ \mu(\mathbf{x}, t) &= \mu_1 + (\mu_2 - \mu_1) I(\mathbf{x}, t). \end{aligned} \quad (2.3)$$

The indicator function, I , is a numerical Heaviside function, ideally zero in one phase and one in the other phase. I is resolved with a sharp but smooth transition across 3 to 4 grid cells and is generated using a vector distance function computed directly from the tracked interface (Shin & Juric 2009).

The fluid variables \mathbf{u} and P are calculated by a projection method (Chorin 1968). The temporal scheme is first order, with implicit time integration used for the viscous terms. For spatial discretization we use the staggered-mesh marker-in-cell (MAC) method (Harlow & Welch 1965) on a uniform finite-difference grid with second-order essentially non-oscillatory (ENO) advection (Shu & Osher 1989). The pressure and distance function are located at cell centers while the x , y and z components of velocity are located at the faces. All spatial derivatives are approximated by standard second-order centered differences. The treatment of the free surface uses a hybrid Front-Tracking/Level-Set technique which defines the interface both by a discontinuous density field on the Eulerian grid as well as by triangles on the Lagrangian interface mesh.

The surface tension \mathbf{F} is implemented by the hybrid/compact formulation (Shin 2007)

$$\mathbf{F} = \sigma \kappa_H \nabla I, \quad \kappa_H = \frac{\mathbf{F}_L \cdot \mathbf{N}}{\mathbf{N} \cdot \mathbf{N}} \quad (2.4)$$

where σ is the surface tension coefficient and κ_H is twice the mean interface curvature field calculated on the Eulerian grid, with

$$\mathbf{F}_L = \int_{\Gamma(t)} \kappa_f \mathbf{n}_f \delta_f(\mathbf{x} - \mathbf{x}_f) ds, \quad \mathbf{N} = \int_{\Gamma(t)} \mathbf{n}_f \delta_f(\mathbf{x} - \mathbf{x}_f) ds \quad (2.5)$$

Here, \mathbf{x}_f is a parameterization of the time-dependent interface, $\Gamma(t)$, and $\delta_f(\mathbf{x} - \mathbf{x}_f)$ is a Dirac distribution that is non-zero only where $\mathbf{x} = \mathbf{x}_f$; \mathbf{n}_f stands for the unit normal vector to the interface and ds is the length of an interface element; κ_f is twice the mean interface curvature obtained on the Lagrangian interface. The geometric information, unit normal, \mathbf{n}_f , and interface element length, ds in \mathbf{N} are computed directly from the Lagrangian interface and then distributed onto the Eulerian grid using the discrete delta function and the immersed boundary method of Peskin (1977). A detailed description of the procedure for calculating \mathbf{F} , \mathbf{N} and I can be found in Shin & Juric (2007).

The Lagrangian interface is advected by integrating $d\mathbf{x}_f/dt = \mathbf{V}$ with a second-order

Runge-Kutta method where the interface velocity, \mathbf{V} , is interpolated from the Eulerian velocity.

The parallelization of the code is based on algebraic domain decomposition, where the velocity field is solved by a parallel generalized minimum residual (GMRES) method for the implicit viscous terms and the pressure by a parallel multigrid method motivated by the algorithm of Kwak & Lee (2004). Communication across process threads is handled by message passing interface (MPI) procedures.

The code contains a module for the definition of immersed solid objects and their interaction with the flow, which we have used to simulate Faraday waves in a spherical container. In order to simulate a fluid within a solid sphere we take the simple approach of defining all grid cells whose centers lie within the solid region as solid. Then the usual velocity and pressure boundary conditions are applied to those cell faces as in the projection method at conventional no-slip domain boundaries. On a Cartesian grid this necessarily creates a stair-stepped solid/fluid boundary; however it is found that the method works well in practice and is simpler than and equivalent to other approaches which impose a near-wall force to ensure a no-slip condition at the solid (Tryggvason *et al.* 2011).

Further details are available in Shin *et al.* (2015).

2.3. Physical and numerical parameters

Our numerical code, like our Floquet analysis, can treat inner and outer spherical domains of any size containing fluids of any density ρ , viscosity ν , and surface tension σ , leading potentially to a large number of non-dimensional parameters, in addition to those describing the forcing amplitude and frequency. We have chosen to limit the parameter space as follows.

The high density ratio $\rho_d/\rho_{\text{out}} = 8 \times 10^4$ between the drop and the outer fluid minimizes the effect of the outer fluid.

The viscosity of both fluids is sufficiently low that the stability diagram approaches that of the Mathieu equation. (One of the conclusions of our companion paper is that the Mathieu equation describes the inviscid Faraday instability even in a spherical geometry.) More specifically, $\nu_d/(R^2\omega)$ is between 0.0003 and 0.0006 for the capillary cases and 0.002 and 0.0006 for the gravitational cases. Thus, the configuration we have simulated is close to an inviscid fluid drop in a vacuum. Usually, Faraday waves are subharmonic, i.e. their period is twice the forcing period T . However, in this low-viscosity regime, we can easily excite harmonic waves as well (Kumar 1996), whose period is the same as the forcing period. Although our thresholds are close to the inviscid ones, the Reynolds number is not large, since the velocity depends on the forcing amplitude a so that $Re \sim aR/(\omega\nu_d) \simeq O(100)$.

The domain is either a cube whose half-side is $5R/3$, or a sphere whose radius is $2R$ inscribed in a cube of half-side $2R$. See figures 2 and 4. In both cases, the mesh is Cartesian. The domain is divided into subdomains, each of which contains 32^3 gridpoints and assigned to a process thread. Unless otherwise stated, our resolution is 64^3 , for which we use $2^3 = 8$ subdomains and processes. For a few cases, we have carried out simulations with a resolution of 256^3 , for which we use $8^3 = 512$ subdomains and processes. Except for the case described in section 3.1, we obtained the same patterns as with the lower resolution. We take about 2000 timesteps per forcing period T .

For some of our simulations, the initial condition for the interface is a sphere perturbed only by its representation on a triangular mesh as described in section 2.2; this is the condition designated as spherically symmetric in table 1. In other cases, the sphere is perturbed according to one of the formulas given by Busse (1975). Axisymmetric initial

Temporal ℓ Response	Initial Condition	Forcing Amplitude	Frequency	Final Pattern
	Gravitational	a/a_g	ω/ω_g	
1 subharmonic	spherically symmetric	0.26	1.96	Translational
2 harmonic	axisymmetric	0.50	1.37	Prolate-Oblate
	Capillary	a/a_c	ω/ω_c	
3 subharmonic	spherically symmetric	13.53	13.21	Tetrahedral
4 subharmonic	spherically symmetric	5.07	16.61	Cubic-Octahedral
5 subharmonic	axisymmetric	22.00	25.02	D_4
6 subharmonic	icosahedral	16.07	30.63	Cubic-Octahedral

TABLE 1. Parameters of imposed forcing and of the observed response.

conditions are of the form

$$\zeta - R \propto Y_\ell^0 + \text{c.c.} \quad (2.6)$$

where c.c. means complex conjugate. In all cases, the initial velocity is zero.

Table 1 lists the simulations which we will describe in this paper. We study either gravity or capillary waves, i.e. a Bond number $\rho g R^2 / \sigma$ of either infinity or zero. Figure 1 locates the parameter values that we have used for our simulations within the instability tongues for the gravitational or capillary cases, where

$$\omega_g^2 \equiv \frac{g}{R} \quad \omega_c^2 \equiv \frac{\sigma}{\rho R^3} \quad (2.7a)$$

$$a_g \equiv R\omega_g^2 = g \quad a_c \equiv R\omega_c^2 \quad (2.7b)$$

See Ebo Adou & Tuckerman (2015) for more details on this non-dimensionalization. (For our low-viscosity cases, the tongues are very close to the inviscid ones; we plot the inviscid tongues for simplicity.) Frequencies are chosen to induce instabilities from $\ell = 1$ to $\ell = 6$, as predicted from linear Floquet theory. In each case, the value of ℓ from the full three-dimensional nonlinear direct simulations agrees with the theoretical value.

2.4. Spherical harmonic transform

In order to analyze the shape of the drop quantitatively, we present its time-dependent spectral coefficients, both $|\zeta_\ell^m(t)|$ from (1.1) and

$$|\zeta_\ell(t)| = \left[\sum_{m=0}^{\ell} |\zeta_{\ell,m}(t)|^2 \right]^{1/2} \quad (2.8)$$

We calculate the spherical harmonic transform as follows. The three-dimensional Lagrangian interface consists of triangles composed of points (x_i, y_i, z_i) on the Cartesian grid. We transform each of these points to spherical coordinates $(\zeta_i, \theta_i, \phi_i)$. We interpolate the function $\zeta(\theta_i, \phi_i) = \zeta_i$ onto a regular spherical grid (θ_j, ϕ_k) , discretizing the latitudinal interval $[0, \pi]$ and longitudinal interval $[0, 2\pi]$ with $N_\theta = 80$ and $N_\phi = 80$ points. Using the discrete data $\zeta(\theta_j, \phi_k)$ and truncating the series (1.1) at four times the

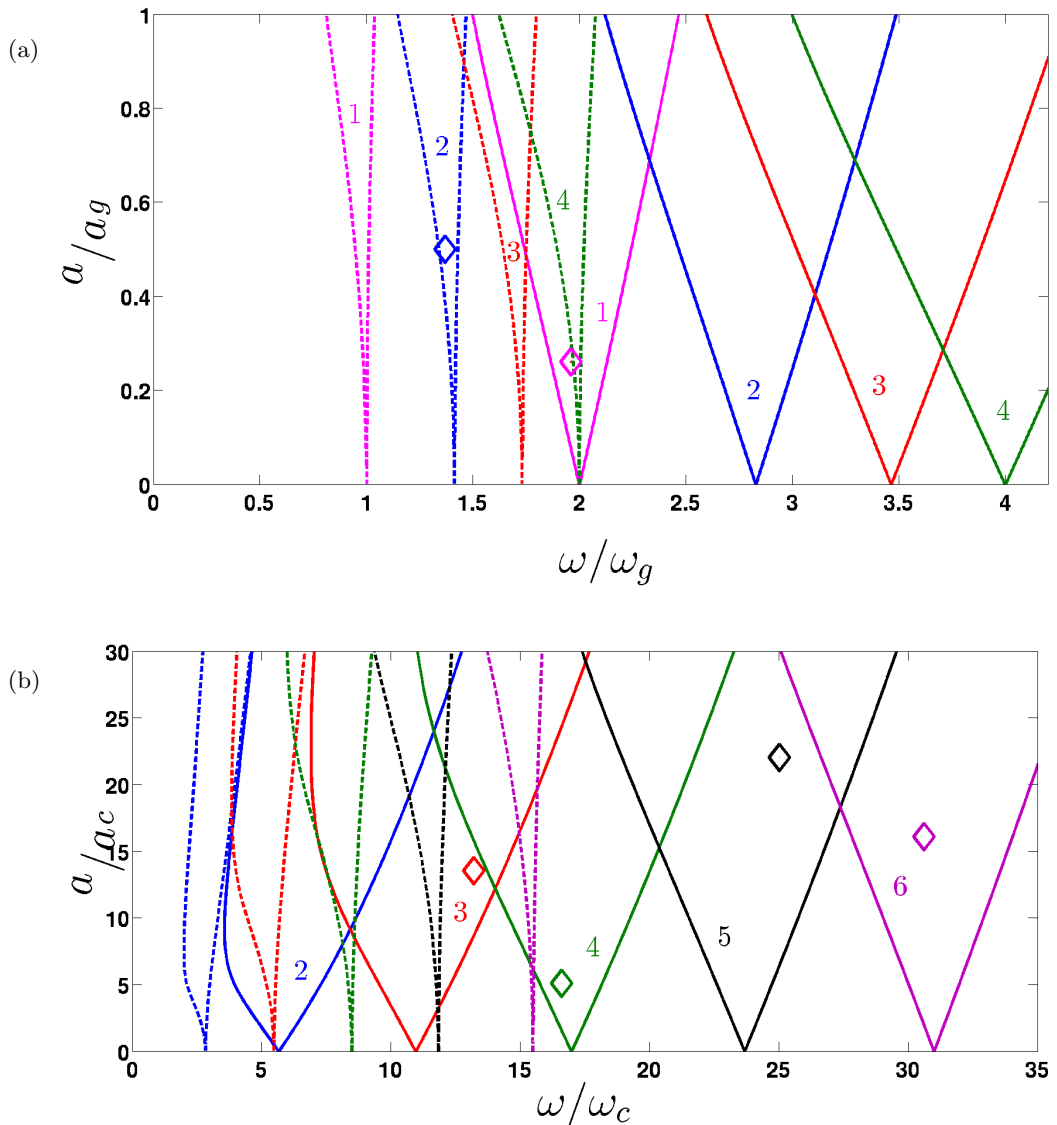


FIGURE 1. Instability tongues resulting from oscillatory forcing with amplitude a and angular frequency ω for an inviscid drop with parameters given in table 1. Diamond shapes designate the parameter values of our simulations. Solid curves bound subharmonic tongues and dashed curves bound harmonic tongues. (a) Tongues corresponding to gravitational instability with spherical wavenumbers $\ell = 1, 2, 3, 4$ originate at $\omega/\omega_g = 2\sqrt{\ell}/n$, with $n = 1$ for subharmonic tongues and $n = 2$ for harmonic tongues. (b) Tongues corresponding to capillary instability with spherical wavenumbers $\ell = 2, 3, 4, 5, 6$ originate at $\omega/\omega_c = 2\sqrt{\ell(\ell-1)(\ell+2)}/n$.

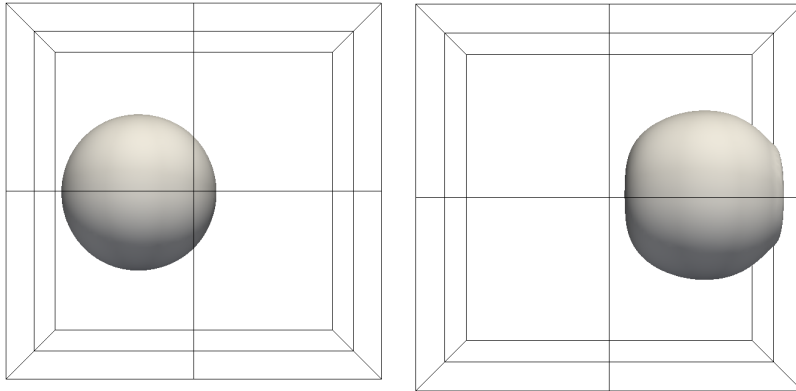


FIGURE 2. Visualization of $\ell = 1$ mode for drop. The drop is displaced alternately to the left and the right, and finally hits the surface of the domain. The cubic domain is shown, as well as the eight subdomains, each of which is assigned to a process thread.

dominant value of ℓ , we compute the spherical harmonic coefficients ζ_ℓ^m by the method of least squares (Politis 2013). This procedure is carried out for each sampled temporal snapshot of the interface.

The spectrum in m (but not in ℓ) depends on the orientation. We can rotate a pattern by localizing the coordinates (θ, ϕ) of one of its features, such as a maximum, rotating in longitude ϕ to place it in the (x, z) plane and then rotating in colatitude θ to place this feature at the north pole. This allows us to interpret our spectra by using the explicit representations given by Busse (1975) of various patterns in terms of Y_ℓ^m . Conversely, if the shape of the pattern is known or constant, the spectrum in m can be used to track its orientation, and changes in its orientation.

3. Results

3.1. Case $\ell = 1$

We study the $\ell = 1$ case in the purely gravitational regime, i.e. in the presence of a constant radial force $g\mathbf{e}_r$, included in the time-periodic force (2.2), and without surface tension. Our simulations of this case exhibit a periodic subharmonic translational motion of the sphere about its original position, as shown in figure 2. This explains why the $\ell = 1$ case is prohibited for capillary waves: translational motion does not involve deformation of the interface, and so surface tension cannot act as a restoring force. The oscillations increase in amplitude until the drop hits the boundary of the cubic domain; despite decreasing the excitation amplitude, we have thus far been unable to obtain an asymptotic regime.

The subharmonic tongue for $\ell = 1$ overlaps with the harmonic tongue for $\ell = 4$ over a range of forcing frequencies; see figure 1. When the driving parameters lie in this region, we find that the mode obtained depends on the numerical resolution. For a resolution of 64^3 we obtain subharmonic $\ell = 1$ oscillations, while for a resolution of 256^3 the harmonic $\ell = 4$ solution is obtained, but will not be presented here.

As stated by Busse (1975), there is no competition between different patterns in this case. All solutions are obtained by rotation of a single axisymmetric pattern, which is expected to be stable. (The three spherical harmonics Y_1^1, Y_1^0, Y_1^{-1} are also related by rotation.)

3.2. Case $\ell = 2$

To produce a case in which $\ell = 2$ is the dominant mode, we have simulated harmonic oscillations in the gravitational regime. A sequence of figures from our numerical simulations showing the shape and velocity field at the interface is shown in figure 3 and figure 4, which also shows the velocity field in the outer fluid. The interface remains axisymmetric and spheroidal, with two principal axes of the same length, and a third of a different length. Figure 3(a) shows a prolate shape, like a rugby ball (the third axis is longer than the other two), while the shape in figure 3(c) is oblate, like a disk (the third axis is shorter). During the prolate phase, the velocity is directed in the polar direction, while during the oblate phase it is directed in the equatorial direction. At maximum deformation, the velocity changes direction, so that the velocity is minimum when the surface is most deformed and maximum when it is least deformed. Because the interface is opaque, velocity vectors directed inwards cannot be seen.

Oblate-to-prolate oscillations have been studied extensively (Trinh & Wang 1982; Tsamopoulos & Brown 1983; Patzek *et al.* 1991). These authors observe that the drop spends a longer time in the prolate than in the oblate configuration. Figure 5 shows the amplitude $|\zeta_{\max} - \zeta_{\min}|$ as a function of time. The prolate and oblate configurations are represented by higher and lower maximum values of $|\zeta_{\max} - \zeta_{\min}|$, respectively. We observe that the drop spends about 60% of each period in the prolate configuration, in agreement with the literature (Trinh & Wang 1982; Tsamopoulos & Brown 1983; Patzek *et al.* 1991).

We present the results of the spherical harmonic transform of the interface height $\zeta(\theta, \phi, t)$. Figure 6 shows the time evolution of the amplitude of ζ_ℓ , defined in (2.8). The most visible feature of figure 6 is its rapid oscillation. In order to examine the dynamics on larger timescales, we extract the envelope of each ζ_ℓ , as shown by the bold curves in figure 6. There is no variation in ζ_0 , since this is the mean radius, and cannot change due to incompressibility. Although $\ell = 2$ is the dominant non-zero spherical wavenumber for this case, other even ℓ (multiples of 2) are also present. These wavenumber multiples $n\ell$ are generated by nonlinear interactions which also multiply the growth rates and frequencies by the same factor of n .

Although we began our simulations by perturbing the sphere with an axisymmetric initial condition, proportional to $Y_2^0 + \text{c.c.}$, the drop orientation quickly tilted away from the z axis, acquiring components with $m \neq 0$, while remaining axisymmetric about its own axis. The symmetry axis continues to oscillate periodically, with alternating phases in which $m = 2$ and then $m = 1$ dominates, as shown in figure 7.

We have also obtained prolate-oblate oscillations in simulations (not presented here) of subharmonic capillary waves with an axisymmetric initial condition.

According to Busse (1975); Chossat *et al.* (1991), the only allowed solution for $\ell = 2$ is axisymmetric, and is unstable at onset. Our observation of a stable asymptotic regime does not contradict this result since our parameter values are far from onset.

3.3. Case $\ell = 3$

For $\ell = 3$, there exist solutions with three possible symmetries: axisymmetric, D_6 , and tetrahedral. Either the D_6 or the tetrahedral solution can be stable at onset (Busse 1975; Chossat *et al.* 1991). Our solution for this case has tetrahedral symmetry, as can be seen in figure 8, which shows subharmonic capillary oscillations. The initial condition is a slightly perturbed sphere, but the same behavior is seen starting from an initial condition proportional to Y_3^0 . Over a half oscillation period, the tetrahedron in figure 8(a) reverses its orientation, as shown in figure 8(c), since this polyhedron is self-dual.

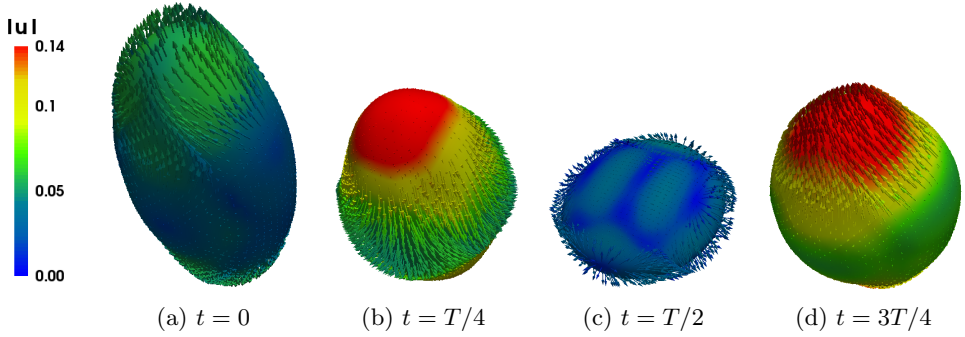


FIGURE 3. Drop interface and velocity field for $\ell = 2$ pattern of gravitational harmonic waves over one reponse period T . During the prolate phase, the velocity is directed in the polar direction, while during the oblate phase it is directed in the equatorial direction. Colors indicate the magnitude of the velocity, which is maximal when the surface is least deformed and minimal where it is most deformed. Only outward-point velocity vectors are shown; those pointing inwards are hidden by the opaque surface of the drop.

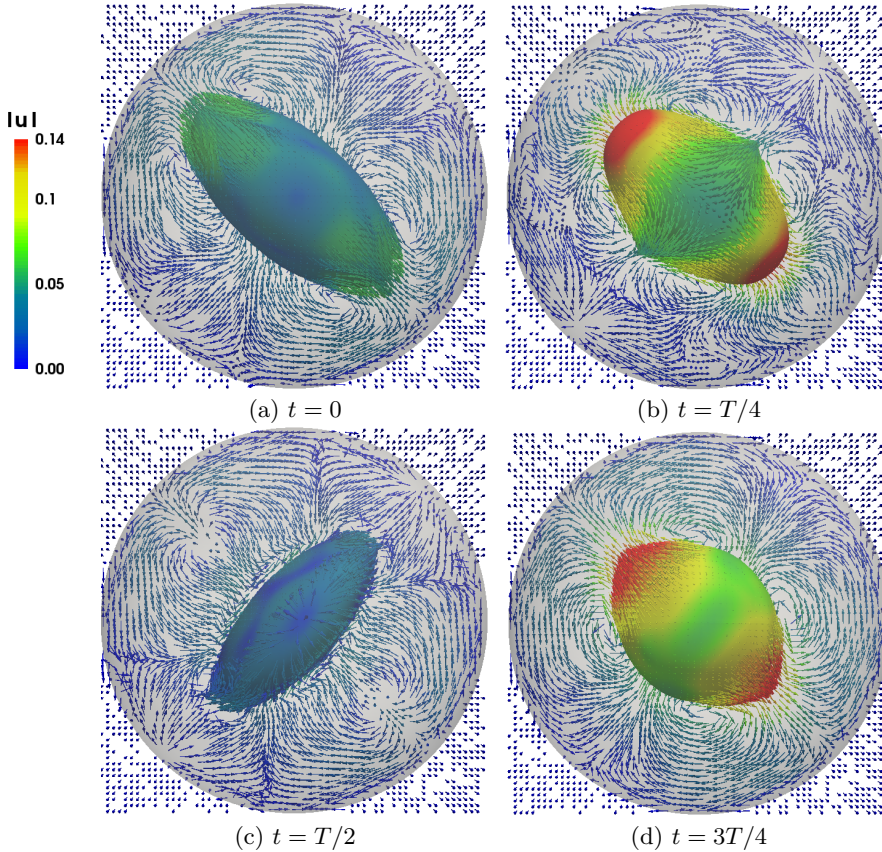


FIGURE 4. Same as figure 3 but from a slightly different perspective and showing the outer bounding sphere and the velocity field in the outer fluid.

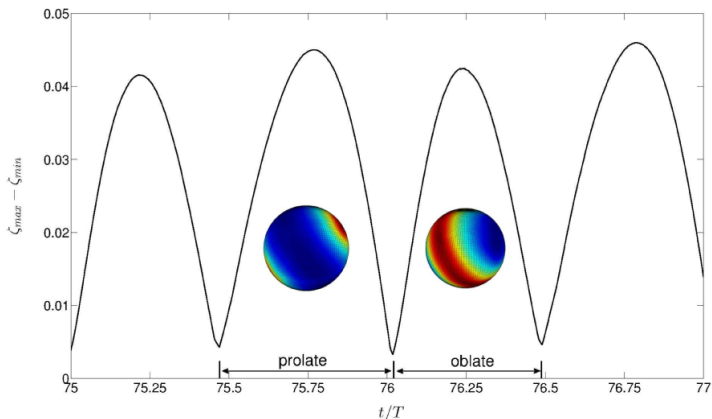


FIGURE 5. Timeseries of interface amplitude $|\zeta_{\max} - \zeta_{\min}|$ for $\ell = 2$. Insets show the projection of the height $\zeta(\theta, \phi)$ on the sphere. Prolate and oblate configurations have higher and lower maximum values of $|\zeta_{\max} - \zeta_{\min}|$, respectively. The drop spends about 60% of each period in the prolate configuration.

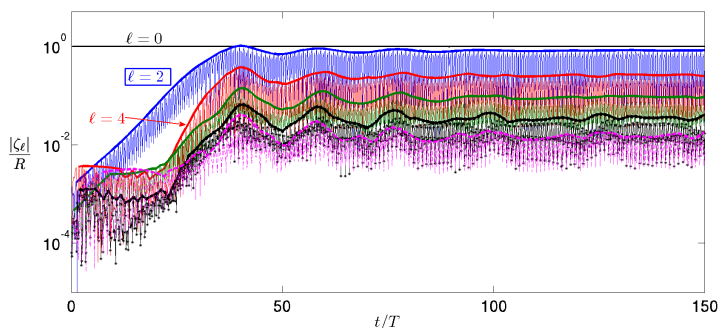


FIGURE 6. Timeseries of components of different ℓ modes when the dominant mode is $\ell = 2$ (indicated by the boxed label). All multiples of $\ell = 2$ are present, as well as $\ell = 0$, which is the constant average radius. Long-time evolution is visualized by envelopes (bold curves) of the rapidly oscillating timeseries. The growth rate of component ζ_4 is about twice that of ζ_2 .

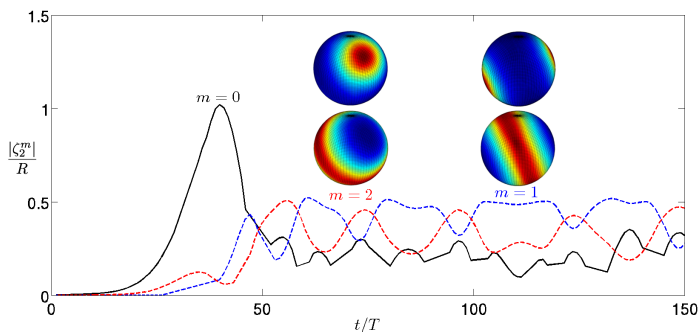


FIGURE 7. Timeseries of components of various m modes, when the dominant mode is $\ell = 2$. Initially, the drop is axisymmetric and the only component is $m = 0$. The drop remains axisymmetric, but its axis of symmetry tilts away from the z axis, which continues to oscillate periodically, manifested by alternating dominance of $m = 1$ and $m = 2$.

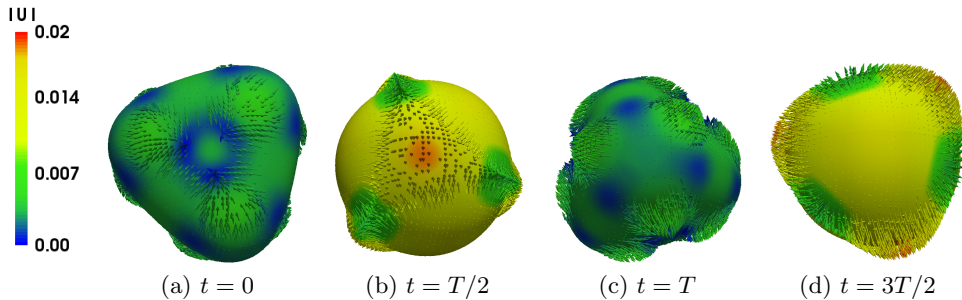


FIGURE 8. Drop interface and corresponding velocity field for $\ell = 3$ pattern seen in subharmonic capillary waves over one reponse period $2T$. Colors indicate the magnitude of the velocity, which is maximal when the surface is least deformed and minimal where it is most deformed. Only outward-pointing velocity vectors are shown; those pointing inwards are hidden by the opaque surface of the drop.

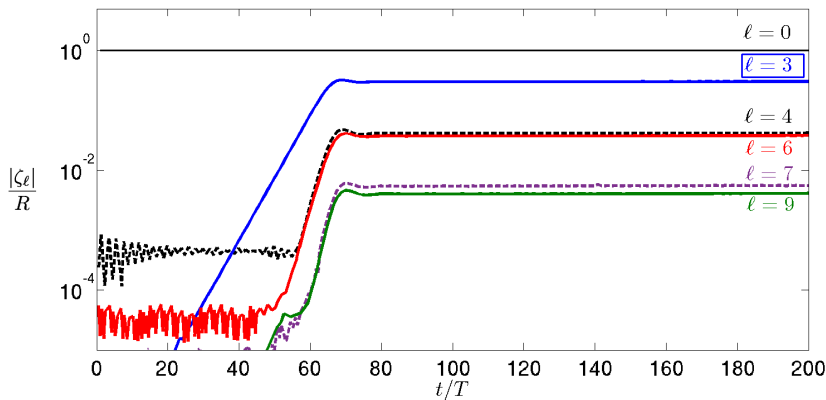


FIGURE 9. Time evolution of the amplitudes of modes with different ℓ values. The principle mode is $\ell = 3$. The amplitude of mode $\ell = 4$ is very close to that of the second harmonic $\ell = 6$, and that of $\ell = 7 = 3 + 4$ is close to that of the third harmonic $\ell = 9$.

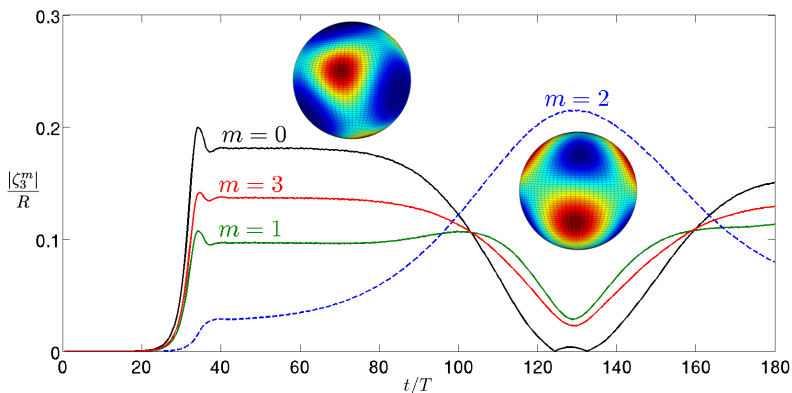


FIGURE 10. Time evolution of the amplitudes of ζ_3^m . The initial position of the pattern is tilted with respect to the z axis. As the $m = 2$ component increases, the pattern aligns with the z axis. It then decreases as the pattern tilts again.

The pattern contains ℓ components other than $\ell = 3$, as illustrated in figure 9. In particular, an important $\ell = 4$ component is present, more specifically $(\ell, m) = (4, 0)$ and $(4, 4)$, which will be seen in figure 13 to compose a cube. These components may be due to the Cartesian grid, since they are present even in a domain bounded by an immersed sphere rather than a cubic box.

Initially, the pattern is not aligned with the domain, but, over long times, it tilts to become aligned with the z axis. This is illustrated in figure 10, since

$$\zeta - R \propto Y_3^2 + \text{c.c.} \quad (3.1)$$

corresponds to a tetrahedron aligned with the z -axis (Busse 1975). Subsequently, the pattern again tilts out of alignment.

3.4. Case $\ell = 4$

When $\ell = 4$, the preferred solution possesses octahedral/cubical symmetry O (Busse 1975; Matthews 2003). Visualizations of our numerical simulations of subharmonic capillary oscillations are shown in figure 11. Two initial conditions, axisymmetric or a perturbed sphere, gave similar results. We have also obtained a cubic pattern in simulations (not presented here) of harmonic gravitational waves with a spherical initial condition and a resolution of 256^3 . The pattern oscillates between resembling a cube, with six square faces, of which three meet at each vertex, and resembling its dual, the octahedron with eight equilateral triangles, four of which meet at each corner.

Figure 12 shows that, in addition to $\ell = 4$ and its harmonics, the ℓ wavenumber spectrum contains a large $\ell = 6$ component, along with its harmonics, and modes resulting from interactions between the $\ell = 4$ and $\ell = 6$ families. We observe that the pattern is always aligned with the numerical domain, with two faces or minima (for the cube) or two vertices or maxima (for the octahedron) located at the north and south poles. With this alignment, Busse (1975) gives a construction of a cubic solution as a sum of zonal and sectoral modes:

$$\zeta - R \propto \sqrt{7} Y_4^0 + \sqrt{5} Y_4^4 + \text{c.c.} \quad (3.2)$$

The time evolution of ζ_4^0 and ζ_4^4 during our simulation is shown in figure 13.

Bifurcation theory predicts two possible solutions at onset (Busse 1975; Chossat *et al.* 1991), with axisymmetric or cubic symmetry, produced by a transcritical bifurcation and with neither branch stable at onset. Our simulations are far from the threshold, so it is likely that secondary bifurcations have taken place which stabilize existing branches and create new ones.

3.5. Case $\ell = 5$

The theoretical analysis of the $\ell = 5$ case is the most complicated of those surveyed here (Busse & Riahi 1982; Riahi 1984), since it leads to eight allowed solutions with different symmetries (Chossat *et al.* 1991). Figures 14 and 15 show gravitational subharmonic oscillations, starting from an initial condition which is an axisymmetric perturbation of the sphere, proportional to Y_5^0 . The solution is at first axisymmetric, as shown in figure 14, but is eventually replaced by another solution with D_4 symmetry, shown in figure 15. The pattern remains aligned with the z axis. The upper hemisphere contains four patches of outward (inward) flow, and the lower hemisphere contains four similar patches, located at longitudes which are halfway between those of the patches of the upper hemisphere. This pattern corresponds to the preferred solution **F** described by Riahi (1984):

$$\zeta - R \propto \sqrt{3} Y_5^0 + \sqrt{5} Y_5^4 + \text{c.c.} \quad (3.3)$$

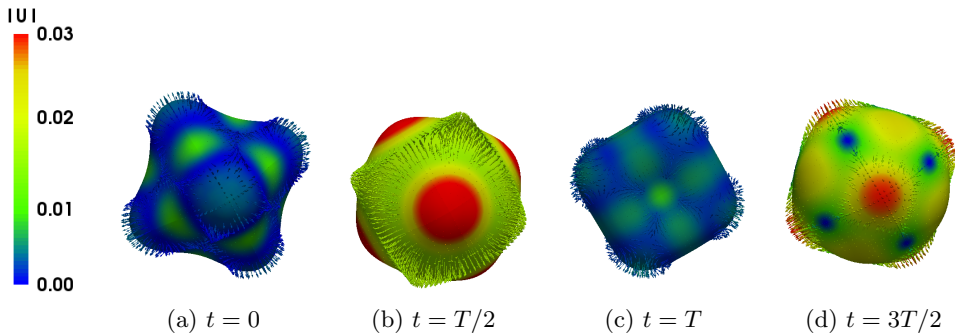


FIGURE 11. Drop interface and velocity field for $\ell = 4$ pattern seen in subharmonic capillary waves over one reponse period $2T$. The interface oscillates between (a) an octahedron, with six maxima, and (c) a cube, with eight maxima. Colors indicate the magnitude of the velocity, which is maximal (minimal) when the surface is least (most) deformed. Only outward-pointing velocity vectors are shown.

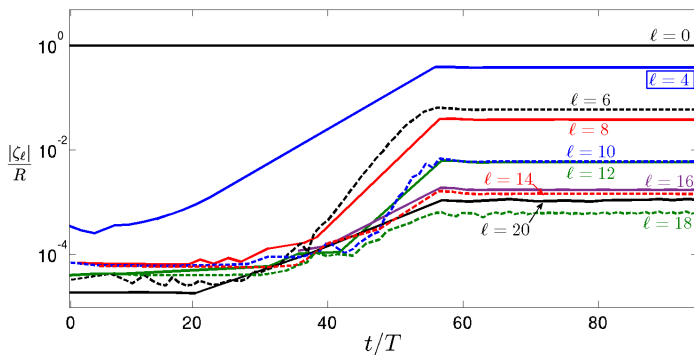


FIGURE 12. Time evolution of amplitude of different ℓ components when the dominant wavenumber is $\ell = 4$. The spectrum also contains an important $\ell = 6$ component. The spectrum contains multiples of 4, multiples of 6, and combinations of the two ($10=4+6$, $14=8+6$, $20=8+12$).

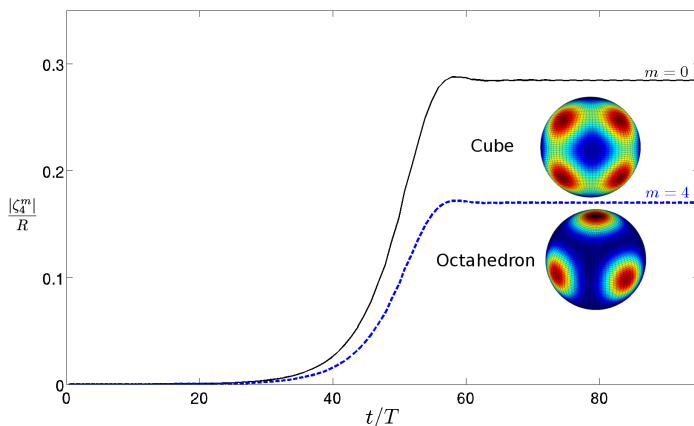


FIGURE 13. Evolution of amplitudes of important modes $m = 0$ and $m = 4$, which together comprise the pattern with cubical symmetry for $\ell = 4$. Inset shows projection of height on the sphere at instants at which the interface has a cubic or octahedral shape. The alignment with the z axis can be seen, for example by the red patch at the north pole (where the longitudinal gridlines meet) for the octahedron.

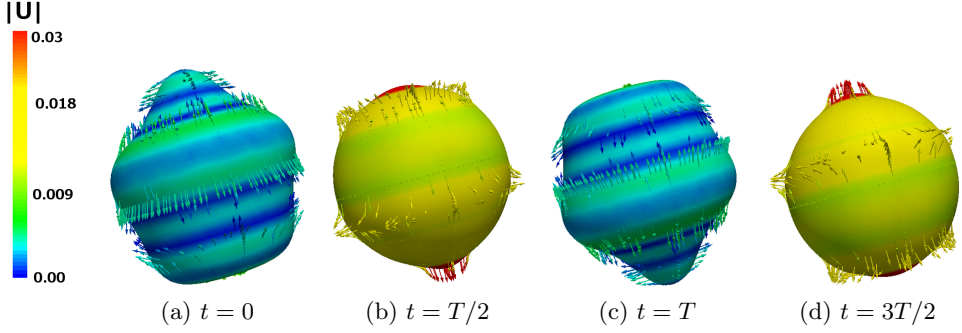


FIGURE 14. Drop interface and corresponding velocity field for axisymmetric $\ell = 5$ pattern seen in subharmonic capillary waves over one reponse period $2T$. Colors indicate the magnitude of the velocity, which is maximal (minimal) when the surface is least (most) deformed. Only outward-pointing velocity vectors are shown.

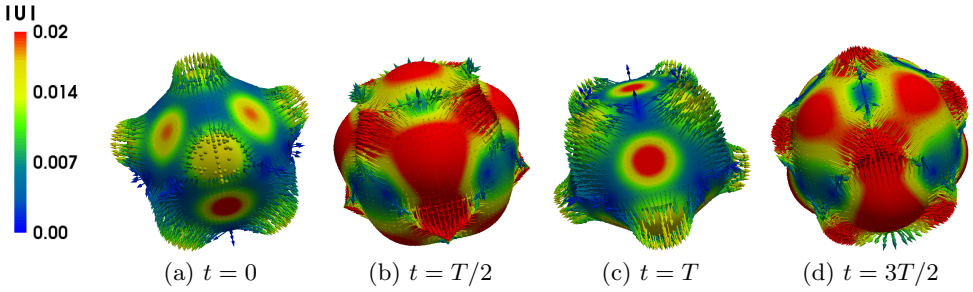


FIGURE 15. Drop interface and corresponding velocity field for $\ell = 5$ pattern with D_4 symmetry.

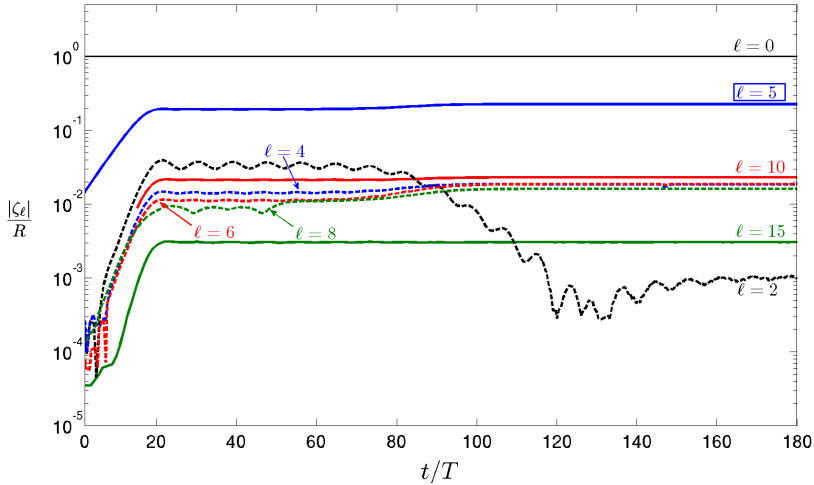


FIGURE 16. Time evolution of the amplitudes of modes with different ℓ values when the dominant mode is $\ell = 5$. Components 4, 6, 8 are present, in addition to the expected multiples of 5.

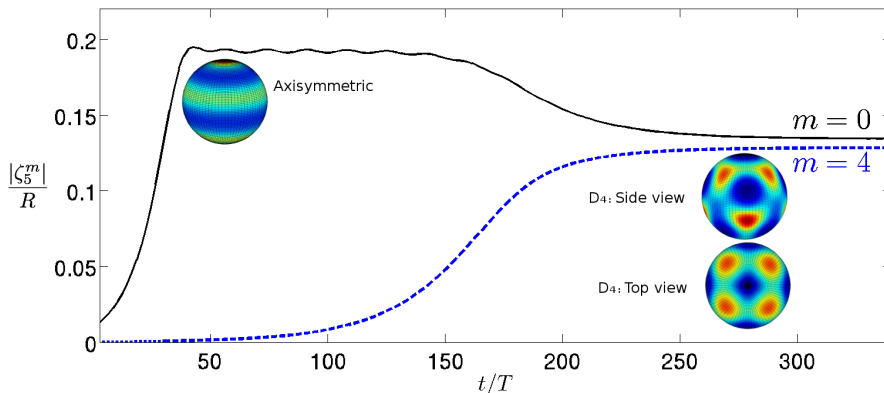


FIGURE 17. Time evolution of the amplitudes of modes Y_5^m . An initially axisymmetric pattern, composed of Y_5^0 , proves to be unstable and is replaced by a D_4 pattern, which is a superposition of Y_5^0 and Y_5^4 . Insets show projections on sphere of $\zeta(\theta, \phi)$ of axisymmetric pattern and two views of D_4 pattern.

Because the pattern remains aligned with the z axis, the transition from an axisymmetric pattern to (3.3) can be tracked by following the different m modes, as is done in figure 17. The initial plateau in ζ_5^0 indicates that the axisymmetric phase of the oscillations shown in figure 14 comprises a solution, albeit unstable, of our system. The later decrease in ζ_5^0 is accompanied by an increase in ζ_5^4 , which together comprise the stable solution with D_4 symmetry.

3.6. Case $\ell = 6$

For $\ell = 6$, there exist four possible solutions: axisymmetric ($O(2)$), six-fold symmetric (D_6) octahedral (O), and icosahedral (I). Of these, the icosahedral solution is preferred, via a maximization argument (Busse 1975) or a stability argument (Matthews 2003). Figures 18 and 19 show subharmonic capillary oscillations carried out in a domain bounded by an outer sphere. The initial condition is an icosahedral perturbation of the sphere (Busse 1975):

$$\zeta - R \propto \sqrt{11} Y_6^0 + \sqrt{14} Y_6^5 + \text{c.c.} \quad (3.4)$$

The first phase of the solution is shown in figure 18, whose five-fold symmetry is clearly visible. Figure 18(a) resembles a dodecahedron, i.e. pentagons which meet in sets of three at the vertices. Figure 18(c) resembles an icosahedron, i.e. triangles which meet in sets of five at the vertices. Further evolution leads to the solution shown in figure 19, which oscillates between a cube and its dual, an octahedron,

Figure 20 shows the time evolution of the spectrum in ℓ for this case, while figure 21 shows the time evolution of the most important m modes associated with $\ell = 6$. The icosahedral pattern, consisting of modes $m = 0$ and $m = 5$, quickly tilts away from the z axis and is then replaced by a cubic pattern, whose dominant mode is $m = 4$. The subsequent increase in $m = 3$ is associated with the tilting of the cubic pattern away from the z axis, rather than a change in the pattern.

Simulations carried out in a cubic domain from a spherical initial condition perturbed only by its discrete representation on a triangular mesh led directly to the cubic/octahedral solution, even when the resolution was increased from 64^3 to 256^3 . The preference for a cubic/octahedral pattern, even from an icosahedral initial condition in a nominally spherical domain, contradicts the theoretical prediction of preference for

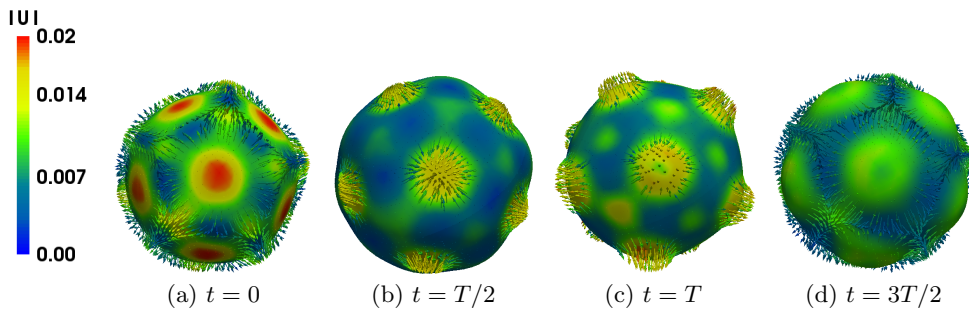


FIGURE 18. Drop interface and corresponding velocity field for $\ell = 6$ pattern with icosahedral symmetry seen in subharmonic capillary waves over one reponse period $2T$. Colors indicate the magnitude of the velocity, which is maximal (minimal) when the surface is least (most) deformed. Only outward-pointing velocity vectors are shown.

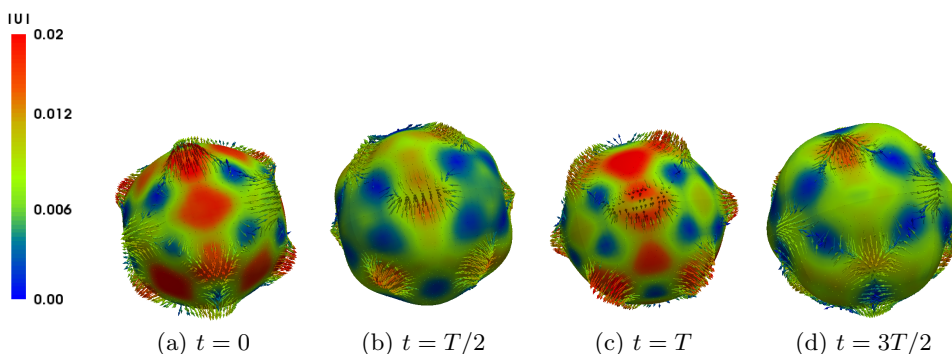


FIGURE 19. Drop interface and corresponding velocity field for $\ell = 6$ pattern with cubic symmetry.

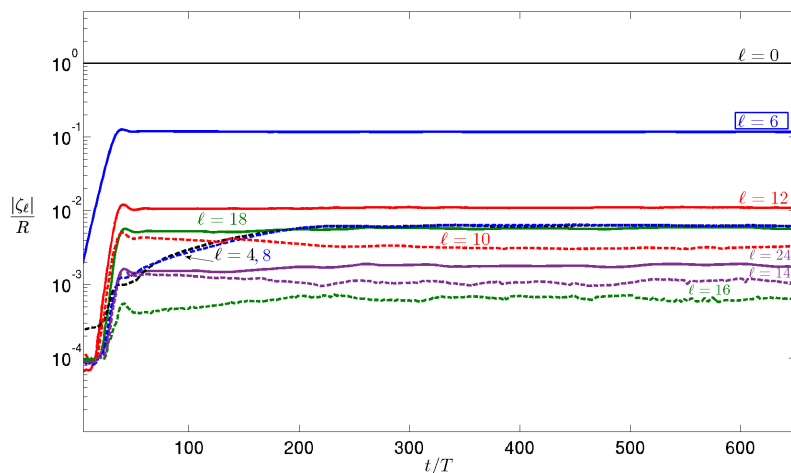


FIGURE 20. Time evolution of the amplitudes of modes with different ℓ values when the dominant mode is $\ell = 6$. In addition to multiples of 6, the spectrum contains multiples of 4 and combinations of the two.

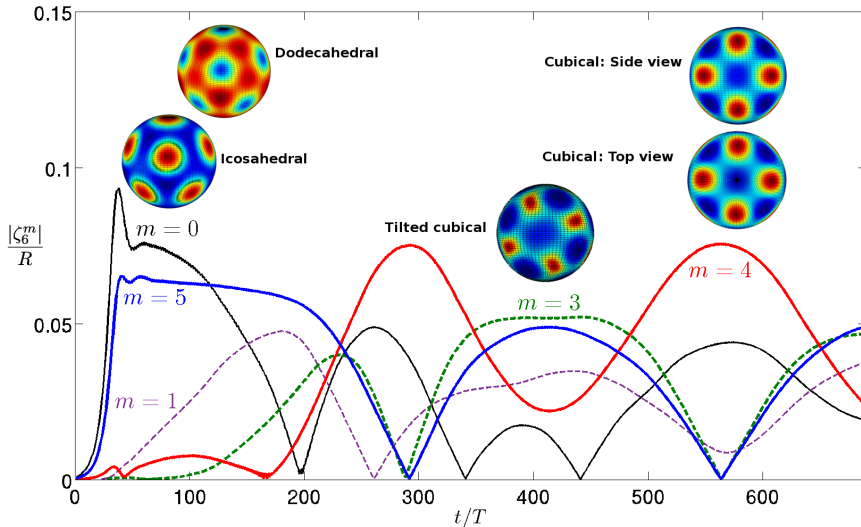


FIGURE 21. Evolution of amplitudes of m modes for $\ell = 6$. From an icosahedral initial condition composed of modes $m = 0$ and $m = 5$, the pattern tilts away from the z axis and eventually acquires cubic symmetry with dominant mode is $m = 4$. The subsequent increase in mode $m = 3$ is associated with a tilting of orientation of the cubical pattern away from the z axis. Insets show projections of icosahedral and dodecahedral phases of the initial pattern, side (equatorial) and top (polar) view of a single cubical pattern aligned with the z axis, and a tilted cubical pattern.

icosahedral patterns and may be due to the residual cubical symmetry of the underlying Cartesian grid.

4. Discussion

Simulating our spherical Faraday problem with the parallel front-tracking code BLUE, we have been able to produce patterns with all spherical harmonic wavenumbers, going from $\ell = 1$ to $\ell = 6$. For $\ell = 1$ and $\ell = 2$, we have simulated the gravitational regime, while for $\ell = 3, 4, 5, 6$, we have simulated capillary waves. Most of our simulations are of the usual subharmonic regime, but we have also been able to simulate harmonic waves in several cases, in particular $\ell = 2$.

Our simulations agree in most cases with two types of theory. First, the spherical harmonic wavenumber ℓ obtained in each case agrees with the results of Floquet analysis, presented in our companion paper (Ebo Adou & Tuckerman 2015) and in figure 1.

Second, the interface shapes we observe are readily interpreted using the theory of pattern formation on the sphere, despite the important differences with our configuration mentioned in the introduction, i.e. the fact that our patterns are oscillatory rather than steady and that our parameters are far above threshold. For $\ell = 1$ and $\ell = 2$, only one type of pattern is possible, and that is the one we observe. For our vibrating drop, the $\ell = 1$ “pattern” is manifested as a back-and-forth motion of the spherical drop, while the $\ell = 2$ pattern alternates between an oblate and a prolate spheroid. For $\ell = 3$, we observe a tetrahedral pattern, one of the two solutions predicted to be stable (out of the three which can exist), while for $\ell = 4$, we observe a cubic/octahedral pattern, one of the two solutions predicted to exist. For $\ell = 5$, we observe an unstable axisymmetric pattern and a stable D_4 pattern. These are two of the eight possible solutions; D_4 is one

of those which can be stable at onset. For $\ell = 6$, the pattern which eventually emerges is cubic/octahedral. It is only in this case that our results differ from theory, which predicts that the icosahedral solution is the preferred solution, while in our case, it is a transient even when it is introduced as the initial condition. We conjecture that this difference may be due to cubical forcing by the underlying Cartesian grid.

It would be interesting to extend the results further by conducting a more detailed bifurcation analysis. We recall that we simulate primarily subharmonic oscillations and, in some cases, harmonic oscillations. For the discrete-time system derived by sampling the continuous-time system at a single phase of the forcing period, harmonic oscillations are fixed points, while subharmonic oscillations are two-cycles. Because of this, harmonic oscillations can result from transcritical bifurcations, while subharmonic oscillations are necessarily associated with pitchfork bifurcations. For even ℓ , bifurcation theory (Matthews 2003) predicts transcritical bifurcations, which cannot occur for subharmonic oscillations. In this sense, bifurcations to harmonic oscillations in our time-periodic system may more closely resemble bifurcations in steady systems.

Another avenue of exploration that has arisen in our study is that of long-term dynamics. The $\ell = 2$ (prolate-oblate), $\ell = 3$ (tetrahedral) and $\ell = 6$ (cubical-octahedral) cases all show the drop tumbling into and out of alignment with the coordinate system, as illustrated in figures 7, 10 and 21. One might expect a cubical pattern to remain aligned with the coordinate system, and it does in the $\ell = 4$ case, but not for $\ell = 6$. It is possible that these long-term dynamics might be permanent, much like those in hexagonal Faraday waves in a minimal domain (Périnet *et al.* 2012).

The spectral analysis of our states demonstrates the complexity of these patterns, since large components which are not multiples of the dominant ℓ are present. Some of these components may result from the Cartesian forcing. Others may provide evidence that the states that we observe are not in fact those produced at the primary bifurcations, but from secondary symmetry-breaking bifurcations that have yet to be explored.

On a practical level, we have demonstrated the feasibility of numerical simulation of an oscillating drop. We believe that the Faraday problem serves as a rigorous proving ground for numerical interface techniques since both qualitative and quantitative comparison of precise quantities is necessary. We hope that this work on the spherical Faraday instability can open up new possibilities in the study of pattern formation and that the numerical code can serve as a useful tool in the exploration of this rich dynamical system.

Acknowledgements

This work was performed using high performance computing resources provided by the Institut du Développement et des Ressources en Informatique Scientifique (IDRIS) of the Centre National de la Recherche Scientifique (CNRS), coordinated by GENCI (Grand Équipement National de Calcul Intensif). L.S.T. acknowledges support from the Agence Nationale de la Recherche (ANR) for the TRANSFLOW project. This research was supported by the Basic Science Research Program through the National Research Foundation of Korea (NRF) funded by the Ministry of Science, ICT and future planning (NRF-2014R1A2A1A11051346).

REFERENCES

- ARBELL, H. & FINEBERG, J. 2002 Pattern formation in two-frequency forced parametric waves. *Phys. Rev. E* **65**, 036224.
- BASARAN, O. A. 1992 Nonlinear oscillations of viscous liquid drops. *J. Fluid Mech.* **241**, 169–198.

- BRUNET, P. & SNOEIJER, J. H. 2011 Star-drops formed by periodic excitation and on an air cushion—a short review. *Eur. Phys. J. Special Topics* **192**, 207–226.
- BUSSE, F. H. 1975 Patterns of convection in spherical shells. *J. Fluid Mech.* **72**, 67–85.
- BUSSE, F. H. & RIAHI, N. 1982 Patterns of convection in spherical shells. part 2. *J. Fluid Mech.* **123**, 283–301.
- CHORIN, A. J. 1968 Numerical simulation of the Navier-Stokes equations. *Math. Comput.* **22**, 745–762.
- CHOSSAT, P., LAUTERBACH, R. & MELBOURNE, I. 1991 Steady-state bifurcation with $O(3)$ symmetry. *Arch. Rational Mech. Anal.* **113**, 313–376.
- DOUADY, S. 1990 Experimental study of the Faraday instability. *J. Fluid Mech.* **221**, 383–409.
- EBO ADOU, A. & TUCKERMAN, L. S. 2015 Faraday instability on a sphere: Floquet analysis. *J. Fluid Mech.* **submitted**.
- EDWARDS, W. S. & FAUVE, S. 1994 Patterns and quasi-patterns in the Faraday experiment. *J. Fluid Mech.* **278**, 123–148.
- FARADAY, M. 1831 On a peculiar class of acoustical figures; and on certain forms assumed by groups of particles upon vibrating elastic surfaces. *Philos. Trans. R. Soc. London* **121**, 299–340.
- FUTTERER, B., KREBS, A., PLESA, A. C., ZAUSSINGER, F., HOLLERBACH, R., BREUER, D. & EGBERS, C. 2013 Sheet-like and plume-like thermal flow in a spherical convection experiment performed under microgravity. *J. Fluid Mech.* **735**, 647–683.
- GOLUBITSKY, M., STEWART, I. & SCHAEFFER, D. G. 1988 *Singularities and Groups in Bifurcation Theory: Vol. II*. Springer-Verlag.
- HARLOW, F. H. & WELCH, J. E. 1965 Numerical calculation of time dependent viscous incompressible flow of fluid with free surface. *Phys. Fluids* **8**, 2182.
- IHRIG, E. & GOLUBITSKY, M. 1984 Pattern selection with $O(3)$ symmetry. *Physica D* **13**, 1–33.
- KAHOUADJI, L., PÉRINET, N., TUCKERMAN, L. S., SHIN, S., CHERGUI, J. & JURIC, D. 2015 Numerical simulation of supersquare patterns in Faraday waves. *J. Fluid Mech.* **772**, R2.
- KUDROLLI, A., PIER, B. & GOLLUB, J. P. 1998 Superlattice patterns in surface waves. *Physica D* **123**, 99–111.
- KUMAR, K. 1996 Linear theory of Faraday instability in viscous fluids. *Proc. R. Soc. Lond.* **452**, 1113–1126.
- KWAK, D. Y. & LEE, J. S. 2004 Multigrid algorithm for the cell-centered finite-difference method ii: Discontinuous coefficient case. *Numer. Meth. Part. Differ. Equ.* **20**, 723–741.
- LUNDGREN, T. S. & MANSOUR, N. N. 1988 Oscillations of drops in zero gravity with weak viscous effects. *J. Fluid Mech.* **194**, 479–510.
- MATTHEWS, P. C. 2003 Pattern formation on a sphere. *Phys. Rev. E* **67**, 036206.
- MERADJI, S., LYUBIMOVA, T. P., LYUBIMOV, D. V. & ROUX, B. 2001 Numerical simulation of a liquid drop freely oscillating. *Cryst. Res. Technol.* **36**, 729–744.
- PATZEK, T., BENNER, R., BASARAN, O. & SCRIVEN, L. 1991 Nonlinear oscillations of inviscid free drops. *J. Comput. Phys.* **97**, 489–515.
- PÉRINET, N., JURIC, D. & TUCKERMAN, L. S. 2012 Alternating hexagonal and striped patterns in Faraday surface waves. *Phys. Rev. Lett.* **109**, 164501.
- PESKIN, C. S. 1977 Numerical analysis of blood flow in the heart. *J. Comput. Phys.* **25**, 220–252.
- POLITIS, A. 2013 Real/complex spherical harmonic transform, Gaunt coefficients and rotations. <http://www.mathworks.com/matlabcentral/fileexchange/43856-real-complex-spherical-harmonic-transform--gaunt-coefficients-and-rotations/>.
- POPINET, S. 1993 Gerris: a tree-based adaptive solver for the incompressible euler equations in complex geometries. *J. Comput. Phys.* **190**, 572–600.
- RAJCHENBACH, J., LEROUX, A. & CLAMOND, D. 2011 New standing solitary waves in water. *Phys. Rev. Lett.* **107**, 024502.
- RIAHI, N. 1984 Nonlinear convection in a spherical shell. *J. Phys. Soc. of Jpn.* **53**, 2506–2512.
- RUCKLIDGE, A. M. & SKELDON, A. C. 2015 Can weakly nonlinear theory explain Faraday wave patterns near onset? *J. Fluid Mech.* **777**, 604–632.
- SHEN, C. L., XIE, W. J. & WEI, B. 2010 Parametrically excited sectorial oscillation of liquid drops floating in ultrasound. *Phys. Rev. E* **81**, 046305.

- SHIN, S. 2007 Computation of the curvature field in numerical simulation of multiphase flow. *J. Comput. Phys.* **222**, 872–878.
- SHIN, S., CHERGUI, J. & JURIC, D. 2015 A solver for massively parallel direct numerical simulation of three-dimensional multiphase flows. *Commun. Comput. Phys.* **submitted**. [arXiv:1410.8568](#).
- SHIN, S. & JURIC, D. 2007 High order level contour reconstruction method. *J. Mech. Sci. Technol.* **21(2)**, 311–326.
- SHIN, S. & JURIC, D. 2009 A hybrid interface method for three-dimensional multiphase flows based on front-tracking and level set techniques. *Int. J. Numer. Methods Fluids* **60**, 753–778.
- SHU, C. W. & OSHER, S. 1989 Efficient implementation of essentially non-oscillatory shock capturing schemes, ii. *J. Comput. Phys.* **83**, 32–78.
- SILBER, M. & PROCTOR, M. R. E. 1998 Nonlinear competition between small and large hexagonal patterns. *Phys. Rev. Lett.* **81**, 2450.
- TRINH, E. & WANG, T. G. 1982 Large-amplitude free and driven drop-shape oscillations: experimental observations. *J. Fluid Mech.* **122**, 315–338.
- TRYGGVASON, G., SCARDOVELLI, R. & ZALESKI, S. 2011 *Direct Numerical Simulation of Gas-Liquid Multiphase Flows*. Cambridge University Press.
- TSAMOPOULOS, J. A. & BROWN, R. A. 1983 Nonlinear oscillations of inviscid drops and bubbles. *J. Fluid Mech.* **127**, 514–537.
- WANG, T. G., ANILKUMAR, A. V. & LEE, C. P. 1996 Oscillations of liquid drops: results from USML-1 experiments in space. *J. Fluid Mech.* **308**, 1–14.